Electronic structure of the frustrated diamond lattice magnet math xmlns="http://www.w3.org/1998/Math/MathML">msub>mi mathvariant="normal">NiRh/mi>mn>2/mn>/msub>msub>mi mathvariant="normal">O/mi>mn>4/mn>/msub>/math>

B. Zager, J. R. Chamorro, L. Ge, F. Bahrami, V. Bisogni, J. Pelliciari, J. Li, G. Fabbris, T. M. McQueen, M. Mourigal, and K. W. Plumb

Electronic structure of the frustrated diamond lattice magnet NiRh$_2$O$_4$

B. Zager,[1] J. R. Chamorro,[2, 3] L. Ge,[4] F. Bahrami,[5] V. Bisogni,[6] J. Pelliciari,[6]
J. Li,[6] G. Fabbris,[7] T. M. McQueen,[2, 3, 8] M. Mourigal,[4] and K. W. Plumb[1]

[1] *Department of Physics, Brown University, Providence, Rhode Island 02912, USA*
[2] *Department of Chemistry, Johns Hopkins University, Baltimore, Maryland 21218, USA*
[3] *Institute for Quantum Matter, William H. Miller III Department of Physics and Astronomy,*
Johns Hopkins University, Baltimore, Maryland 21218, USA
[4] *School of Physics, Georgia Institute of Technology, Atlanta, Georgia 30332, USA*
[5] *Department of Physics, Boston College, Chestnut Hill, Massachusetts 02467, USA*
[6] *National Synchrotron Light Source II, Brookhaven National Laboratory, Upton, New York 11973, USA*
[7] *Advanced Photon Source, Argonne National Laboratory, Lemont, Illinois 60439, USA*
[8] *Department of Materials Science and Engineering,*
Johns Hopkins University, Baltimore, Maryland 21218, USA
(Dated: July 13, 2022)

The A-site spinel NiRh$_2$O$_4$ is the only known realization of a spin-1 diamond lattice magnet and is predicted to host unconventional magnetic phenomena driven by frustrated nearest and next-nearest neighbor exchange as well as orbital degeneracy. Previous works found no sign of magnetic order but found a gapped dispersive magnetic excitation indicating a possible valence bond magnetic ground state. However, the presence of many competing low energy degrees of freedom and limited empirical microscopic constraints complicates further analysis. Here, we carry out resonant inelastic x-ray scattering (RIXS), x-ray absorption spectroscopy (XAS), and inelastic neutron scattering (INS) to characterize the local electronic structure and lattice dynamics of NiRh$_2$O$_4$. The RIXS data can be partly described by a single-ion model for tetrahedrally coordinated Ni^{2+} and indicates a tetragonal distortion $\Delta t_2 = 70$ meV that splits the t_2 orbitals into a high energy orbital singlet and lower energy orbital doublet. We identify features of the RIXS spectra that are consistent with a Rh-Ni two-site excitation indicating strong metal-metal hybridization mediated by oxygen in NiRh$_2$O$_4$. We also identify signatures of electron-phonon coupling through the appearance of phonon sidebands that dress crystal field excitations. These results establish the key energy scales relevant to the magnetism in NiRh$_2$O$_4$ and further demonstrate that covalency and lattice dynamics play essential roles in controlling the magnetic ground states of A-site spinels.

I. INTRODUCTION

Materials with frustrated magnetic interactions provide a platform for realizing novel phases which avoid conventional symmetry-breaking order [1]. Such phases are acutely sensitive to a hierarchy of competing energy scales involving spin, charge, orbital, and lattice degrees of freedom [2]. This enables precise tuning of the collective orders in these systems to explore new phenomena and develop new technologies [3]. Along this line, there has recently been a significant interest in novel phases driven by strong spin orbit coupling (SOC) that has motivated significant work on $4d/5d$ transition metal compounds [4]. In some cases, however, the relatively weak SOC in $3d$ compounds may still become relevant. In particular, when there is an orbital degeneracy, SOC may compete with the Jahn-Teller (JT) effect to produce a spin-orbital-lattice entangled state [5].

The spinel structure comprises an intensely studied class of materials with both fundamental significance and widespread applications. The general formula AB_2X_4 contains tetrahedrally coordinated A^{2+} ions and octahedrally coordinated B^{3+} ions which occupy diamond and pyrochlore sublattices respectively. In the case of magnetic B ions, the system forms a prototypical geometrically frustrated pyrochlore magnet. On the other hand, for magnetic A site ions, the bipartite diamond lattice may be frustrated in the presence of competing nearest and next-nearest neighbor antiferromagnetic exchange [6]. Previously studied diamond lattice magnets include the A-site spinels Co$_3$O$_4$ [7], AAl$_2$O$_4$ (A = Mn, Fe, Co) [8, 9], ASc$_2$S$_4$ (A = Mn, Fe) [10, 11], MnSc$_2$Se$_4$ [12], and ARh$_2$O$_4$ (A = Co, Cu, Ni) [13, 14], as well as the lanthanides LiYbO$_2$ [15] and NaCeO$_2$ [16]. These materials host a variety of magnetic phenomena, ranging from long-range ordered states to disordered spin liquid and spin glass states. In many cases, especially in the presence of an orbital degree of freedom, these materials lie near a quantum critical point, with multiple competing phases exhibiting strong sensitivity to disorder and external perturbations [17–25]. It is thus essential to characterize the microscopic energy scales associated with the spin, lattice, and orbital degrees of freedom in these materials.

Another topic of recent interest is frustrated magnetism in spin-1 materials [26–28], which support more degrees of freedom than spin-$\frac{1}{2}$, while still being sensitive to quantum fluctuations. In particular, recent studies have predicted spin-1 diamond lattice antiferromagnets to host unconventional magnetic phenomena, namely topological paramagnetism [29], spiral spin liquid phases [30], quantum critical phenomena [31], and excitonic magnetism [32].

The spinel NiRh$_2$O$_4$ contains spin-1 Ni^{2+} ions on the

A sites and nonmagnetic Rh^{3+} ions on the B sites, thus realizing the only known spin-1 on a diamond lattice. Early studies identified a cubic to tetragonal structural transition at 390 K [33] and an apparent antiferromagnetic transition at $T_N = 18$ K [34]. However, a recent study on high quality samples found no sign of magnetic order down to 0.1 K [14], implying that chemical disorder may have stabilized ordering found in the original studies. In that study, specific heat and x-ray diffraction measurements found a small entropy loss associated with the structural distortion at $T = 440$ K, indicating only a partial lifting of orbital degeneracy. This finding is consistent with the $p_{\text{eff}} = 3.3\mu_B$ paramagnetic moment that is significantly larger than the pure spin-1 value of $2.83\mu_B$, implying an orbital contribution to the magnetism. The Curie-Weiss temperature of $\Theta_{\text{CW}} = -11$ K indicates a large frustration parameter $f = \Theta_{\text{CW}}/T_N > 100$. Inelastic neutron scattering (INS) found gapped dispersive magnetic excitations suggestive of a valence bond ground state [14]. However, an incomplete knowledge of the electronic ground state has limited modeling of the INS data. Recent theoretical work predicted that spin-orbit coupling, crystal fields, and correlations generate a spin-orbital singlet ground state in $NiRh_2O_4$ [32, 35]. Such a state would explain the absence of magnetic ordering and key features of the magnetization, specific heat, and neutron data. But measurements of the high energy excitations characterizing the orbital configurations of $NiRh_2O_4$ are required to confirm this picture.

In this paper, we use a combination of resonant inelastic x-ray (RIXS), x-ray absorption spectroscopy (XAS), and inelastic neutron scattering to provide a detailed account of the electronic structure of $NiRh_2O_4$. We observe crystal field excitations for Ni^{2+} in a distorted tetrahedral environment that are well-described by a single-ion model including Coulomb interaction, spin-orbit coupling, crystal field splitting. We find additional electronic excitations corresponding to two-site Rh to Ni charge transfer. We also find that the orbital excitations are coupled to optical phonons giving rise to distinct phonon sidebands that dress d-d excitations. These results provide a detailed description of the local electronic structure of a novel frustrated magnet along with the key energy scales required for understanding the magnetic ground state and low-energy excitations. We have additionally shown that both covalency and lattice dynamics play essential roles in this material and should be considered in any realistic model for the magnetism. These insights provide guidance for exploring novel effects in $NiRh_2O_4$ and other magnetically frustrated spinels using pressure, magetic fields, and chemical substitution.

This paper is organized as follows. In section II, we describe the experimental details. In section III, we present the RIXS, XAS, and INS results and describe our attempts to model the data. We first use a single ion model for Ni^{2+} in a distorted tetrahedral crystal field, then a minimal two-site Ni-Rh hopping model, and finally we incorporate electron phonon coupling in order to capture

the lineshapes of the RIXS spectra. Our findings are summarized in section IV.

II. EXPERIMENT

Polycrystalline $NiRh_2O_4$ was synthesized following the methods described in [14]. The samples contain 4% nonmagnetic Rh_2O_3 by mass, which is not expected to contribute any observable effects to our measurements.

Resonant inelastic x-ray scattering (RIXS) measurements at the Ni L_3 edge were performed at the soft inelastic x-ray scattering (SIX) beamline 2-ID at the National Synchrotron Light Source II (NSLS-II) at Brookhaven National Laboratory. Measurements were carried out at 40 K and 25 K using an incident x-ray polarization in both linear horizontal (π) and linear vertical (σ) geometries. The scattering angle was fixed at 90° to minimize the contribution from Thomson elastic scattering and giving a momentum transfer of $Q = 0.61$ Å^{-1}. The incident x-ray energy was varied across the Ni L_3 edge ($\sim$853 eV). The combined energy resolution was determined to be 31 meV based on the full width at half maximum (FWHM) of the elastic signal from carbon tape.

X-ray absorption spectroscopy (XAS) measurements at the O K edge were performed at NSLS-II beamline 2-ID (SIX), measured in fluorescence yield (FY). XAS measurements at the Rh L edges at Advanced Photon Source 4-ID-D, measured in total electron yield (TEY).

Inelastic neutron scattering (INS) measurements were performed on the Fine Resolution Fermi chopper spectrometer (SEQUOIA) at the Spallation Neutron Source, Oak Ridge National lab. The incident neutron energy was fixed at 160 meV using the coarse resolution chopper (FC2) rotating at 600 Hz. The same 4 g sample used in [14] was loaded in an aluminum can, and held at 3.6 K for the measurement. Scattering contributions from the sample environment were removed by subtraction of an empty can data set during data reduction.

III. RESULTS

Fig. 1(b) shows the RIXS intensity as a function of incident energy E_{in} and energy loss ΔE measured at 25 K with incident π polarization. The XAS, shown in white, contains a weak pre-edge feature at 852.9 eV, a main peak split into two features at 853.4 eV and 853.8 eV, and a satellite peak at 856.4 eV. The RIXS spectrum shows an elastic line at $\Delta E = 0$ eV, five Raman-like features at 0.065 eV, 0.25 eV, 0.5 eV, 1.1 eV, and 1.6 eV, a broad charge-transfer (CT) background between 2 and 4 eV, and a fluorescence line (FL) at constant scattered photon energy.

Fig. 1(c) shows RIXS scans at the main resonance of $E_{\text{in}} = 853.4$ eV, indicated by the dotted line in Fig. 1(b), in both π and σ incident polarization at 40 K. The inset shows the low energy region near the elastic line. The
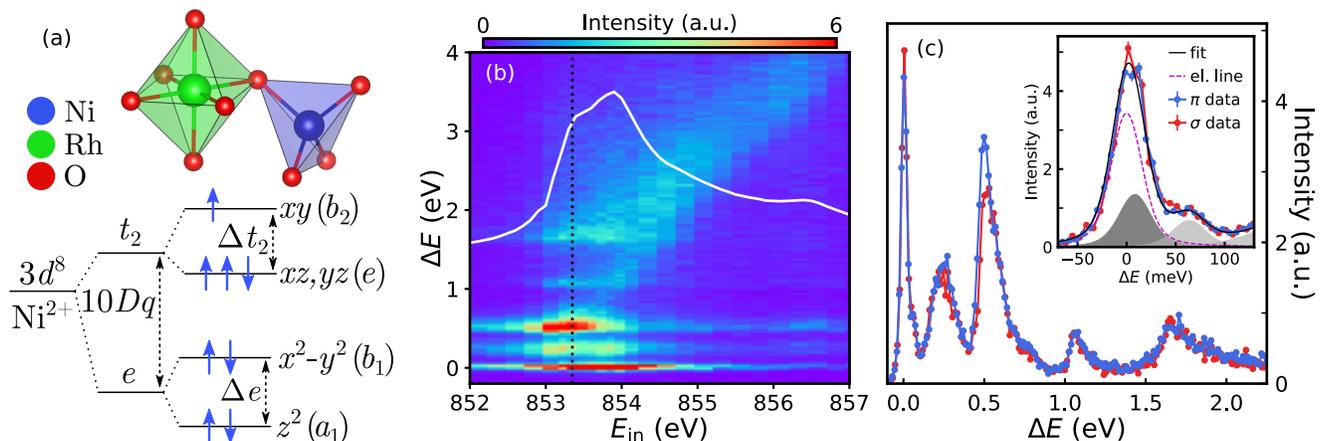
FIG. 1. Overview of Ni L_3 edge RIXS data measured at $T = 40$ K and $2\theta = 90°$. (a) Local coordination of Ni and Rh in NiRh$_2$O$_4$. Rh is octahedrally coordinated while Ni^{2+} $3d$ orbitals are split by tetrahedral crystal field with tetragonal distortion $\Delta t_2 > 0$. (b) Measured RIXS intensity vs. energy loss and incident energy measured in π polarization. The XAS measured in total fluorescence yield is plotted in white. (c) RIXS spectrum in both π and σ polarization at $E_{in} = 853.4$ eV, indicated by the dashed line in (b). The inset shows the low-energy part of the spectrum and an empirical fit.

elastic intensity due to Thomson scattering is expected to be strongly suppressed in the π-polarized data for the 90° scattering angle configuration of these measurements. However, the π and σ-polarized data show similar intensity around $\Delta E = 0$, suggesting unresolved low energy excitations. The elastic line cannot be fit by a single resolution-limited Voigt function, further indicating the presence of unresolved low energy contributions. This can be explained by the $\sim$12 meV dispersive magnetic excitation observed in inelastic neutron scattering [14]. By including an additional resolution-limited Voigt function at 12 meV, we obtain an adequate fit to the quasi-elastic line, as shown in the inset of Fig. 1(c) for the π-polarized data, which also includes contributions from two overlapping higher energy peaks. A similar fit can be obtained for the σ-polarized data, with a slightly larger contribution from the elastic peak likely originating from Thomson scattering that contributes in that geometry.

A. Single-ion model

To identify the features in the measured spectra, we calculate the RIXS cross section for a single Ni^{2+} ion including Coulomb interaction, spin-orbit coupling (SOC), and crystal field (CF) splitting. Calculations were implemented using the EDRIXS package [36], further details are described in the Supplemental Material [37]. We include onsite Coulomb interactions as parameterized by the Slater integrals: F_{dd}^2, and F_{dd}^4 describe the direct Coulomb repulsion between d electrons, F_{pd}^2 describes direct Coulomb repulsion between d electrons and the $2p$ core hole, and G_{pd}^1 and G_{pd}^3 describe the Coulomb exchange between d electrons and the $2p$ core hole. Initial values for the above parameters are calculated for a free

Ni^{2+} ion in $3d^8$ and $2p^5 3d^9$ configurations by the Hartree-Fock method using Cowan's code [38]. To account for the reduced intra-atomic repulsion due to covalency effects in the solid, we include empirical scale factors on F_{dd}, F_{pd}, and G_{pd} that are determined by fitting to the RIXS data.

The crystal-field is parameterized by the tetrahedral splitting $10Dq < 0$ and the splitting due to the tetragonal distortion $\Delta t_2 = E_{b_2} - E_{e'}$, $\Delta e = E_{b_1} - E_{a_1}$. The tetrahedral crystal field (T_d point group) splits the d^8 configuration into $e^4 t_2^4$. The tetragonal distortion ($T_d \rightarrow D_{2d}$) further splits the e doublet into a_1 (d_{z^2}) and b_1 ($d_{x^2-y^2}$) singlets, and the t_2 triplet into a b_2 (d_{xy}) singlet and e' (d_{xy}, d_{yz}) doublet, as shown in Fig. 1(a). These symmetry considerations leave the sign and magnitude of the splittings unconstrained. There have been no reported direct measurements of the crystal field splitting in NiRh$_2$O$_4$, and there are conflicting reports of the sign of the tetragonal splitting. This splitting cannot be constrained only from knowledge of the crystal structure because expectations from electrostatic considerations are often inaccurate due to additional effects from covalency and spin-orbit coupling [2]. As we will show below, both effects are significant in NiRh$_2$O$_4$.

The low temperature structure reported in [14] is tetragonal with elongated NiO$_4$ tetrahedra and compressed RhO$_6$ octahedra. This led the authors to propose a crystal field scheme with the t_2 levels split into a lower b_2 state and upper e' states ($\Delta t_2 < 0$), following the model from [39], as expected from electrostatic considerations. However, the DFT calculation in [35] suggests that the t_2 levels are split into lower e' states and an upper b_2 state ($\Delta t_2 > 0$). We find that although a single ion model fails to reproduce the 0.25 eV peak, the asymmetric lineshapes of the high energy peaks, and the polarization dependence of the quasielastic peak, it en-
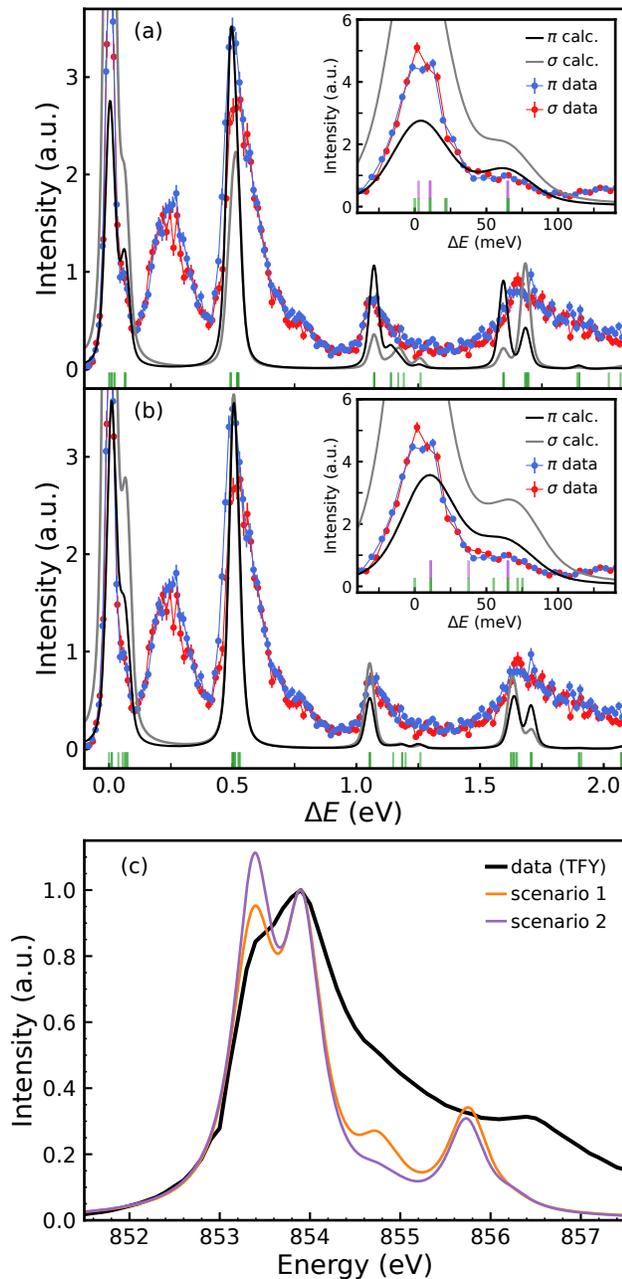
FIG. 2. Comparison of the two crystal field schemes used for modeling the RIXS data. Scenario 1 ($\Delta t_2 > 0$) is shown in (a) and scenario 2 ($\Delta t_2 < 0$) is shown in (b). The green ticks indicate the eigenvalues. The purple ticks in the inset indicate which eigenvalues are dipole-allowed transitions from the ground state for comparison to the neutron data [14]. (c) Comparison of the two schemes for modeling the Ni L_3 XAS (TFY). The calculated XAS spectra are normalized to the intensity at the maximum of the measured spectrum.

TABLE I. Parameters for the single-ion model using $\Delta t_2 > 0$ and $\Delta t_2 < 0$. $10Dq$, Δt_2, Δe, and λ are in meV. F_{dd}, F_{pd}, and G_{pd} are dimensionless.

	$10Dq$	Δt_2	Δe	λ	F_{dd}	F_{pd}	G_{pd}
$\Delta t_2 > 0$	-580	70	56	13	0.5	0.7	0.75
$\Delta t_2 < 0$	-530	-50	-40	27	0.5	0.7	0.75

material trends for insulating Ni compounds and with other spectroscopic measurements on NiRh$_2$O$_4$ [39, 40]. The peaks around 0.5 eV and 1 eV fix the value of $10Dq \approx 0.55$ eV, as they correspond to $e^4 t_2^4 \to e^3 t_2^5$ and $e^4 t_2^4 \to e^2 t_2^6$ transitions. This $10Dq$ value is consistent with DFT [35] and the values for tetrahedrally coordinated Ni^{2+} in other compounds [39]. We can also constrain the value of atomic spin-orbit coupling λ by the requirement of a dipole-allowed level near 11 meV to agree with the neutron scattering data [14]. Finally, the peak at 1600 meV corresponds to an excitation within the Hund's multiplet and fixes the value of F_{dd}. To match the energy of the highest energy peak, F_{dd} must be set to 0.5, giving a Hund's coupling of $J_H = \frac{1}{14}(F_{dd}^2 + F_{dd}^4) = 0.71$ eV. This parameter also sets the energy of intra-t_2 spin-flip excitations ($S = 1 \to S = 0$) between 1.1 and 1.3 eV. These excitations have minimal intensity in the computed RIXS cross section and we do not expect to observe them above the signal-to-noise of our data, see Fig. 2 (a) and (b). The 50% reduction in the intra-atomic Coulomb interaction F_{dd}, compared with the atomic values, suggests strong Ni-O covalency [41] and already indicates the inadequacy of a single ion model for NiRh$_2$O$_4$, we address this later in section III B. The Slater integrals F_{pd} and G_{pd} determine the intermediate state energies and do not affect the RIXS peak energies. However, they do influence the RIXS intensities and energy splitting of the main XAS peak. We have tested models for tetrahedral compression and elongation and find that they both capture many features of the data; table I shows the best parameters for the two scenarios (1) $\Delta t_2 > 0$ and (2) $\Delta t_2 < 0$, plotted in Fig. 2. Δe is underdetermined by our data and mainly contributes to the splitting of the peaks above 500 meV. Here, we assume that Δe has the same sign as Δt_2. We also expect $|\Delta e| < |\Delta t_2|$, due to the reduced Ni-O hybridization of the e states compared to the t_2 states in tetrahedral symmetry. We find that the constraint $\Delta e = 0.8 \Delta t_2$ provides an adequate agreement with the data as shown in Fig. 2. Both models reproduce the observed peaks at 65 meV, 0.5 eV, 1 eV and 1.6 eV and while scenario 1 better reproduces the small dichroism of the 0.5 eV feature, scenario 2 more faithfully reproduces the negligible dichroism of the 1 eV and 1.6 eV peaks. The high energy excitations, $\Delta E > 500$ meV, are far above the insulating gap in NiRh$_2$O$_4$ and are thus coupled to delocalized states. This effect is not captured in the single-ion model and may explain the Fano-like lineshape. However, we found that a more careful examination of the low energy excitations for $E < 100$ meV

ables us to distinguish the two crystal field scenarios and place useful constraints on the magnitudes of tetragonal splitting and spin orbit coupling.

We constrain our model to maintain consistency with

enables a distinction between crystal field models.

The low energy part of the spectrum is shown in the insets of Fig. 2 (a) and (b), with the purple markers indicating energy levels with nonvanishing neutron cross section. Since photons emitted with energies close to the absorption edge are more likely to be reabsorbed, we expect strong self absorption effects near the elastic line and our model should predict a larger quasi-elastic intensity than what is observed. The observed intensities are also likely modified by intersite magnetic exchange interactions [35] that are not included in our single site model. Nevertheless, a careful comparison of the observed linear dichroism at low energy transfers reveals that scenario 1, $\Delta t_2 > 0$, is more consistent with our data. The low energy subspace of scenario 1 is equivalent to the model from [35], and yields excited states at 3^*, $11(2)^*$, $22(2)$, and $65(3)^*$ meV. The low energy subspace of scenario 2 is equivalent to the model from [39], yielding excited states at $11(2)^*$, 38^*, 55, $65(2)^*$, 72, and 75 meV. Asterisks indicate those states with nonvanishing neutron intensity and parentheses indicate the state degeneracy, disregarding any splitting of less than 1 meV. The calculation for scenario 1 shows that the dominant contribution to the quasi-elastic RIXS intensity comes from the ground state and a 3 meV excitation for both polarizations [Fig. 2 (a)]. This is consistent with the nearly equivalent quasielastic lines we measured for each polarization. However, for scenario 2, the dominant contribution comes from the ground state for σ polarization and from the 11 meV excitation for π polarization [Fig. 2 (b)]. Although the energies of these excitations fall within our experimental resolution, scenario 2 should result in a more pronounced difference in the quasielastic lineshape between σ and π polarizations and that is not consistent with our data.

To provide an additional check for our single ion model, we compare with the measured x-ray absorption spectrum (XAS) at the Ni L_3 edge measured in total fluorescence yield (TFY) shown in Fig. 2(c). The main XAS peak is split into lower and upper peaks at 853.4 and 853.8 eV, corresponding to the states $2p^5e^4t_2^5$ and $2p^5e^3t_2^6$. In the single-ion model, this splitting depends on $10Dq$, F_{pd}, and G_{pd}. Although the XAS lineshape is known to be distorted by TFY measurements, the calculated spectrum shows better qualitative agreement with our data for scenario 1. In particular, a model with $\Delta t_2 > 0$ more faithfully reproduces the relative intensities of the 853.4 and 853.8 eV peaks, and captures additional observed intensity at 854.7 eV that is not predicted by a model with $\Delta t_2 < 0$ [Fig 2 (c)]. However, we find that for either scenario, the single-ion model cannot capture the large, ~ 3 eV, splitting between the main peak and satellite peak at 856.4 eV.

Based on the above considerations, we conclude that scenario 1, splitting the t_2 levels into lower energy d_{xz}, d_{yz} orbitals and a higher energy d_{xy} orbital, is the correct crystal field scheme in NiRh$_2$O$_4$. However, there are many notable discrepancies between the single ion model and our data. First, a single-ion model completely fails
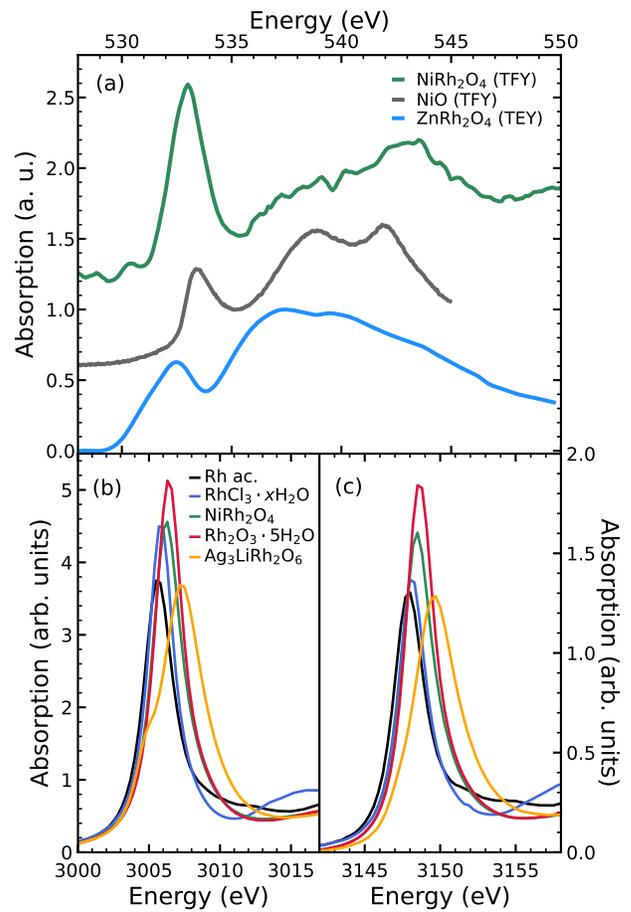
FIG. 3. (a) XAS at the O K edge for NiRh$_2$O$_4$ (TFY), with NiO (TFY) and ZnRh$_2$O$_4$ (TEY) for comparison (NiO data from [42] and ZnRh$_2$O$_4$ data from [43]) (b) XAS measured at the Rh L_3 edge and (c) the Rh L_2 edge.

to reproduce the intense 250 meV RIXS peaks for any reasonable set of parameters [37], and second, it does not accurately capture the broad asymmetric lineshape of the 0.5 eV peak. Both of these features in the RIXS spectra arise because of two distinct effects that cannot be accounted for in a single-ion description. First, there is strong Ni-Rh hybridization, and second, there is strong electron-phonon coupling. The evidence for each of these effects and a detailed discussion of their respective influence on the RIXS spectra and magnetism in NiRh$_2$O$_4$ is discussed below in sections III B and III C.

B. Ni-Rh hybridization

We now extend our model to include the influence of electronic hybridization between Ni and Rh sites. Such metal-metal hybridization is supported both by experiment and ab-initio calculations. Density functional theory calculations [35] have found strong Ni-Rh hybridiza-

TABLE II. Table of peak positions and widths in eV extracted from the Rh L edge XAS by fitting a Lorentzian + arctangent lineshape.

	E_{L3}	E_{L2}	Γ_{L3}	Γ_{L2}
Rh acetate	3005.5(1)	3147.7(1)	2.0(1)	1.8(2)
$RhCl_3 \cdot xH_2O$	3005.7(1)	3148.0(1)	1.8(1)	1.6(2)
$NiRh_2O_4$	3006.1(1)	3148.3(1)	2.0(1)	1.7(2)
$Rh_2O_3 \cdot 5H_2O$	3006.3(1)	3148.5(1)	1.9(1)	1.7(2)
$Ag_3LiRh_2O_6$	3007.0(1)	3149.4(1)	3.0(2)	2.4(3)

tion is mediated by the intermediate oxygens. Furthermore, the calculation found an insulating gap of 250 meV, with the highest occupied and lowest unoccupied states having mostly Rh and Ni character respectively. This suggests that the lowest interband transition consists of Rh→Ni excitations.

We have carried out x-ray absorption (XAS) measurements at the O K and Rh L edges in order to characterize the electronic states at the Rh and O sites in $NiRh_2O_4$. Fig. 3(a) shows the O K edge XAS for $NiRh_2O_4$ measured in total fluorescence yield (TFY), with the spectra for NiO (TFY) and $ZnRh_2O_4$ (TEY) shown for comparison. NiO provides a comparison to bonding in an NiO_6 octahedron while $ZnRh_2O_4$, being isostructural to the cubic phase of $NiRh_2O_4$, provides a comparison to bonding in a RhO_6 octahedron in the absence of an unfilled neighboring $3d$ shell.

The pre-edge region contains a small peak at 530.5 eV and a large peak at 533 eV, corresponding to O $2p$ states hybridized with empty metal d states. The region above 535 eV corresponds to Ni $4sp$ and Rh $5sp$ states. By comparing to the projected density of states from DFT calculations [35], we can assign the small pre-edge peak at 530.5 eV to the unfilled Ni t_2 states and the large peak at 533 eV to the unfilled Rh e_g states. The pre-edge peak intensity is determined by both the number of empty metal states and the degree of hybridization [44]. In NiO and $ZnRh_2O_4$, where the metal sites provide two empty states per O site, the pre-edge peak intensities are comparable. In $NiRh_2O_4$, there are 2 empty Rh states and 0.5 empty Ni states per O site. This small increase in the number of available states alone cannot explain the significant enhancement of pre-edge peak intensity. The intensity can thus be explained by an increased hybridization due to the cooperative influence of the Ni and Rh. This can be expected based on the large inductive effect of Rh^{3+} [45]. It may also be enhanced due to the long range exchange interactions. In the five-site exchange pathway A-O-B-O-A via a nonmagnetic B cation, the dominant contribution is thought to involve the empty states at the B sites [46–48].

Fig. 3(b) and Fig. 3(c) show the XAS at the Rh L_3 and L_2 edges respectively, for $NiRh_2O_4$ and reference samples with known valence: Rh acetate (2+), $RhCl_3 \cdot xH_2O$ (3+), $Rh_2O_3 \cdot 5H_2O$ (3+), $Ag_3LiRh_2O_6$ (4+) [49]. The sharp white line peaks correspond to transitions from $2p$ core levels to empty $4d$ states. The Rh^{2+} and Rh^{3+} spectra
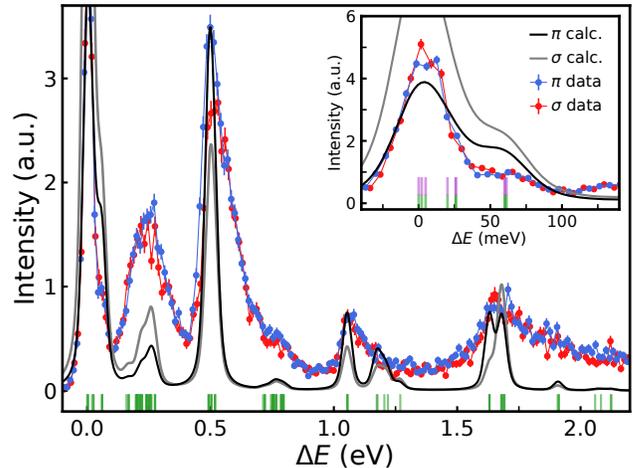
FIG. 4. Calculated RIXS spectrum from the two-site model with $t = 30$ meV, $\Delta = -600$ meV compared with measured data. The green ticks indicate the eigenvalues. The purple ticks in the inset indicate which eigenvalues are dipole-allowed transitions from the ground state for comparison to the neutron data [14].

contain a single peak at each edge, while the Rh^{4+} spectrum contains a shoulder on the low energy side, corresponding to the empty t_{2g} state. As expected, this shoulder is suppressed at the L_2 edge [50]. To quantify the Rh valence, we obtain the white line peak position for each compound from a fit to a Lorentzian plus arctangent lineshape [51, 52]. The results of this fit are summarized in table II. The reference compounds for Rh^{3+} show a 0.6 eV (0.5 eV) difference in peak position at the L_3 (L_2) edge. The higher peak position of Rh_2O_3 compared to $RhCl_3$ can be attributed to the larger covalency of the Rh-O bond compared to the Rh-Cl bond, giving a more delocalized charge density around the Rh site in Rh_2O_3 [53]. We find that the peak position for $NiRh_2O_4$ lies between these two compounds with no significant differences between lineshapes and peak widths. This confirms that despite the strong hybridization, Rh maintains the charge distribution of the 3+ oxidation state with no signs of charge disproportionation, which often occurs in mixed 3d/4d compounds [54–56].

Having confirmed the strong Ni-Rh hybridization and Rh oxidation state in $NiRh_2O_4$, we assign the RIXS peak at 250 meV to a two-site orbital excitation from Rh t_{2g} to Ni t_2, corresponding to the transition Ni $3d^8$ + Rh $4d^6 \rightarrow$ Ni $3d^9$ + Rh $4d^5$. This assignment is corroborated by our effective two site model discussed below. Although such metal-metal charge transfer (MMCT) is well known from optical studies of spinel ferrites [57, 58], there are few reports of these features seen in RIXS [59–61].

A full microscopic description of MMCT in $NiRh_2O_4$ is considerably complicated by the 12 fold nearest neighbor Ni-Rh coordination with intermediate Ni-O-Rh bond angles that prohibit any strict orthogonality constraints

on hopping pathways. In order to capture the essential features of Ni-Rh hybridization present in the RIXS spectra, we construct a minimal model by adding a single set of filled Rh t_{2g} states to the single-ion model from the previous section (see Supplemental Material [37] for details). In this two-site model, the Ni and Rh sites are each subject to Coulomb, crystal field, and spin-orbit interactions, with on-site energy difference Δ and hopping t. Since multiple sites are involved, we now include the monopole part of the Coulomb interaction at each site $U_{Ni} = 6$ eV and $U_{Rh} = 3$ eV. We assume an equal hopping from each Ni t_2 to each Rh t_{2g} and neglect any hopping from the Ni e levels. The effective crystal field parameters obtained from a single-ion model must also be adjusted in the presence of hopping. As shown in Fig. 4, we find good agreement between data and model for the parameters $\Delta = -600$ meV, $t = 30$ meV, $10Dq = -550$ meV, $\lambda = 13$ meV, and $\Delta t_2 = 40$ meV, with the same constraint $\Delta e = 0.8\Delta t_2$. We also set the Rh tetragonal splitting $\Delta t_{2g} = 0$ meV, but the results are mostly unchanged for nonzero Δt_{2g}. This corresponds to scenario 1 discussed above, but similar results are obtained for scenario 2 (see Supplemental Material [37]). We emphasize that the two-site model does not preserve the symmetry of the Ni site, making it ineffective for comparing the two scenarios. This is evident from the inset of Fig. 4, where all low-energy levels have non-negligible dipole character.

Despite the simplicity, the minimal model provides a robust qualitative description of the data, reproducing the energy of all observed RIXS excitations over a 2 eV range of energy transfers with effective parameters describing the approximate energy scales of the Ni-Rh hybridization. A more detailed approach should incorporate the empty Rh e_g levels, which may be essential to the long range exchange interaction, and might consider a double cluster model [62, 63], or symmetry-adapted Rh orbitals [64]. In addition, through comparison of high energy inelastic neutron scattering data that is sensitive to optical phonons, with the RIXS spectra, we find that lattice vibrations enter as an essential energy scale coupled to the electronic states in NiRh$_2$O$_4$. A consideration of electron phonon coupling and vibronic excitations is thus necessary to capture the broad asymmetric lineshape of the RIXS spectra, as discussed in the following section.

C. Electron-phonon coupling

In orbitally degenerate systems, there is a tendency for strong electron-lattice coupling. In many cases, the degeneracy may be lifted by a static lattice distortion via the Jahn-Teller (JT) mechanism [40, 65]. Another possibility is the formation of vibronic modes via the dynamical JT effect, where orbital degeneracy is broken by coupling to lattice vibrations [66]. When the JT distortion energy is comparable to the spin-orbit coupling, the system may host a set of spin-orbital-lattice entangled states [5]. In NiRh$_2$O$_4$, the tetragonal distortion does not
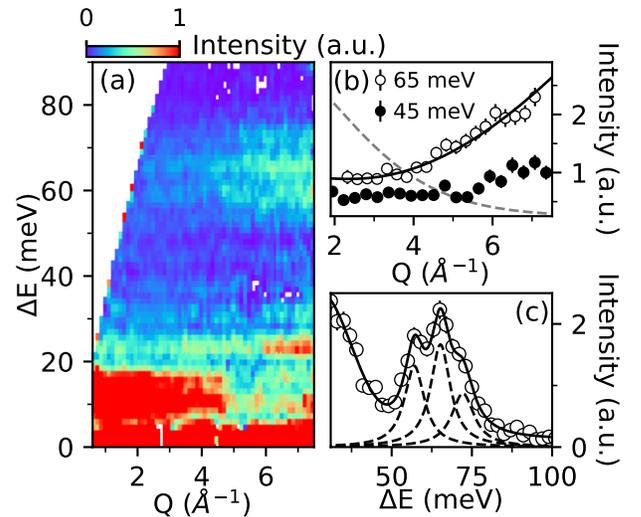
FIG. 5. (a) Inelastic neutron scattering spectra $I(Q, E)$ of NiRh$_2$O$_4$ at $T = 3.6$ K. Collective spin-orbit excitations are visible around 10 meV, and the highest energy optical phonons appear between 60 and 70 meV. (b) Constant energy cuts through $I(Q, E)$ integrated over $E \pm 5$ meV, dashed line shows the momentum dependence of the Ni^{2+} form-factor $|f(Q)|^2$, solid line is a fit to $C|f(Q)|^2 + AQ^2 + B$ as described in the text. (c) Constant momentum-transfer cut integrated over $Q = 6 \pm 1$ Å^{-1}, solid line is a fit to three Lorentzians as described in the text.

fully lift the orbital degeneracy [14]. The weak tetrahedral crystal field splitting (in comparison to octahedral) enables the JT energy to be comparable to SOC. Based on these considerations, we expect lattice dynamics to play a key role in the low-lying spin-orbital excitations.

Here we consider the effects of electron-phonon coupling on the RIXS spectrum of NiRh$_2$O$_4$. Although the RIXS spectra may contain contributions from optical phonons, their precise energies are obscured by the relatively coarse energy resolution on the scale of the phonon energies, and the coincidence of optical phonons with low energy electronic excitations. In order to more precisely quantify optical phonon energies in NiRh$_2$O$_4$, we have re-examined the inelastic neutron scattering data for energies up to 100 meV, covering the full phonon bandwidth. The high energy inelastic neutron scattering data is shown in Fig. 5(a). Below 20 meV, the previously reported collective spin-orbit excitation is visible. As discussed above, this feature was not directly resolved in the RIXS spectra, but accounts for the broadening of the elastic line (inset of Fig. 1(c) and is captured by the single-ion model. At higher energies, we observe optical phonons, centered around 65 meV, coincident with the intra-t_2 excitation in the RIXS spectrum. The quadratically increasing intensity with increasing momentum transfer as shown in Fig. 5(b) indicates that this signal originates primarily from scattering by phonons, but we also find a component attributable to magnetic scatter-

ing. By fitting this cut to $I(Q) = C|f(Q)|^2 + AQ^2 + B$, where $f(Q)$ is the Ni^{2+} magnetic form-factor, A, B, and C are constants, we obtain a good description of the data with the parameters $A = 0.04$, $B = 0.2$, $C = 0.78$. Optical phonon energies were extracted directly from the constant momentum transfer cut in Fig. 5(c). We found that including three Lorentzian functions centered at 57.2(6), 65.3(5), and 72(1) meV and with energy linewidths of $\Gamma = 7.6(1.7)$, 7.5(2.5), and 8.5(2.0) meV respectively was necessary to adequately describe the data. The phonon linewidths are significantly broadened over the instrumental resolution of $\sim$ 4.3-meV Gaussian FWHM at 65 meV. These high energy phonons originate from vibrations of Ni coordinating O tetrahedra, and we expect six distinct modes in this energy range for a cubic cell that are further split in the tetragonal phase [40, 67, 68]. Although the broad phonon lineshapes we observed may be accounted for by unresolved phonon mode splittings, it may also indicate phonon damping caused by coupling to other electronic excitations. Indeed, the coinciding energy of these phonons and the intra-t_2 crystal field excitation measured by RIXS suggests the possibility of a hybridized vibrational-electronic or "vibronic" excitation in $NiRh_2O_4$.

Such electron phonon coupling occurs because the charge distribution of the excited state on Ni repels the surrounding oxygen ions. For the intra t_2 excitation at 65 meV, the extra electron in the d_{xy} orbital is partially screened by the resulting d_{xz}/d_{yz} hole. However, the $e \to t_2$ excitation at 500 meV similarly leaves an extra charge in the t_2 levels, with a hole in the e levels. In this case, we expect the screening to be less effective, and thus the $e \to t_2$ excitation should couple even more strongly to phonons. We can use these considerations to model the lineshape of the 500 meV RIXS peak as a vibronic excitation. Although the single-ion model indicates at least two states comprise this peak and the neutron data shows at least three phonon modes may be involved in the coupling, we will consider a tractable model that includes only a single electronic excitation coupled to a single phonon as such a model is sufficient to capture the essential features of our data. Within this simplified model, we treat the main peak at energy $E_0 = 496$ meV as a bare d-d excitation, or zero-phonon line. This bare dd-excitation is dressed by additional phonon sidebands corresponding to a d-d excitation plus n phonons of energy E_{ph}. We assume a Lorentzian lineshape of FWHM width Γ for each peak separated by energy E_{ph} with relative intensities given by a Poisson distribution [69]

$$I_n = e^{-g}\frac{g^n}{n!},\qquad(1)$$

where g is the dimensionless electron-phonon coupling, which can be interpreted as the mean number of phonons emitted by the excitation. Fig. 6 shows a fit of this minimal model to the 500 meV RIXS peak for $E_0 = 497(2)$ meV, $E_{ph} = 71(2)$ meV, $\Gamma = 60(2)$ meV, and $g = 0.46(3)$ providing an excellent description of the
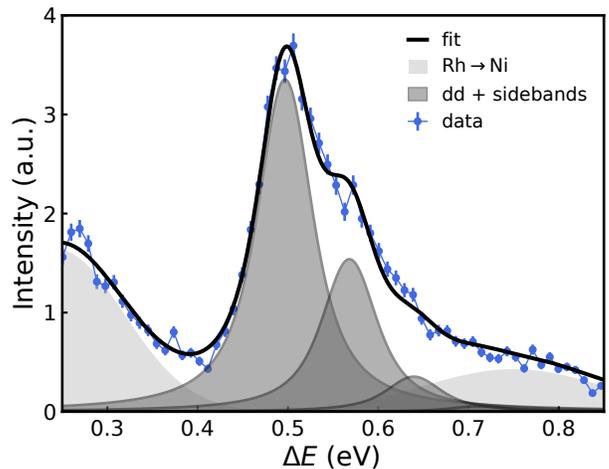
FIG. 6. Poisson model for phonon sidebands fit to the 500 meV RIXS peak, including Gaussian fits to the overlapping neighboring peaks. The phonon sideband cross-section was modeled using equation 1 and Huang-Rhys parameter $g = 0.46(3)$, $\omega_0 = 71(2)$ meV, $E_0 = 497(2)$ meV, and $\Gamma = 60(2)$ meV.

data. The large value of Γ compared to the phonon energies suggests that there are many overlapping excitations within each phonon sideband. This is consistent with the single-ion model for scenario 1 that gives two crystal field excitations, at 492 and 517 meV. Both of these may couple to optical phonons with energies between 57 and 72 meV. A more complete model for electron phonon coupling in $NiRh_2O_4$ would consider the separate d-d excitations and their coupling to multiple phonons, but the resolution of our measurement is not sufficient to constrain such a model.

IV. DISCUSSION AND CONCLUSION

We have characterized the site-specific local electronic structure of $NiRh_2O_4$ using resonant inelastic x-ray scattering and x-ray absorption spectroscopy. We have compared two possible scenarios for the tetragonal splitting within a single ion model and showed that $\Delta t_2 > 0$ is more likely than $\Delta t_2 < 0$, and estimated that $\Delta t_2 = 70$ meV and $\lambda = 13$ meV. These parameters are the most relevant to modeling the magnetism in $NiRh_2O_4$ [32, 35]. The crystal field splittings are in agreement with DFT calculations that determined $\Delta t_2 = 100$ meV and $\lambda = 10$ meV from NMTO downfolding. The single ion model also required a 50% reduction of the F_{dd} Slater parameters, suggesting a significant degree of covalency in $NiRh_2O_4$.

The O K edge XAS data suggests a significant degree of hybridization between O p states and empty metal d states, which can only be explained by a metal-metal charge transfer between adjacent Ni and Rh sites. The

Rh L edge XAS confirmed that the Rh ions maintain the nominal 3+ oxidation state, despite the strong hybridization and tendency toward charge disproportionation in related systems. By extending the RIXS model to include metal-metal charge transfer between Ni and Rh sites as parameterized by an effective hopping $t = 30$ meV, we captured Rh-Ni two-site excitations observed at 250 and 750 meV in the RIXS spectrum. Such an explicit demonstration of the failure of a single ion model and requirement for metal-metal charge transfer in $NiRh_2O_4$ highlights the importance of metal-metal hybridization in mixed 3d-4d/5d compounds in general. This hybridization can affect both the magnetic degrees of freedom and exchange interactions so should be an essential consideration in the design of novel magnetic states in materials such as spinels, double perovskites [70, 71], or $A_2Mo_3O_8$ compounds [28, 72].

A detailed analysis of the RIXS lineshape also revealed that lattice vibrations influence the magnetism in $NiRh_2O_4$ through strong electron-phonon coupling. Inelastic neutron scattering reveals multiple optical phonons overlapping in energy with the intra-t_2 excitation, suggesting a hybridized orbital-lattice excitation between 60 and 70 meV. This effect was observed in the RIXS spectra as a phonon-dressed crystal field excitation at higher energy. Our results provide quantitative constraints on the key parameters for modeling the single-ion ground state and low-lying excitations, as well the long-range superexchange mechanism in $NiRh_2O_4$. We also demonstrate the importance of additional degrees of freedom, namely covalency and phonons, which can alter magnetic ground states [73]. Our results also demonstrate the use of RIXS for probing spin-orbit entangled states in $3d$ transition metal compounds [74] and for probing hybridized states in mixed 3d-4d/5d compounds [75].

In addition to the predicted phenomena associated with spin-1 frustrated diamond lattice antiferromagnets, we propose that $NiRh_2O_4$ may host a variety of novel magneto-elastic and magneto-optical effects due to its rich spectrum of low-energy spin-orbital-lattice excitations [40, 65, 76, 77]. Future studies on $NiRh_2O_4$ could use pressure, magnetic fields or chemical substitution to explore the predicted phase diagram and observe quantum critical phenomena [30–32]. These studies would greatly benefit from the synthesis of single crystals or thin films. Should such crystals become available, another potentially fruitful route would be ultrafast optics to study the spin-orbital and crystal field excitations with the lattice out-of-equilibrium [78–80]. By resonantly exciting the lattice, it may be possible to stabilize an excitonic condensate of $J = 1$ moments [32].

[1] C. Lacroix, P. Mendels, and F. Mila, *Introduction to Frustrated Magnetism: Materials, Experiments, Theory*, Vol. 164 (Springer Science & Business Media, 2011).

[2] D. I. Khomskii, *Transition Metal Compounds* (Cambridge University Press, 2014).

[3] D. Basov, R. Averitt, and D. Hsieh, Nature materials **16**, 1077 (2017).

[4] T. Takayama, J. Chaloupka, A. Smerald, G. Khaliullin, and H. Takagi, Journal of the Physical Society of Japan **90**, 062001 (2021).

[5] S. V. Streltsov and D. I. Khomskii, Phys. Rev. X **10**, 031043 (2020).

[6] V. Tsurkan, H.-A. Krug von Nidda, J. Deisenhofer, P. Lunkenheimer, and A. Loidl, Physics Reports **926**, 1 (2021).

[7] W. Roth, Journal of Physics and Chemistry of Solids **25**, 1 (1964).

[8] N. Tristan, J. Hemberger, A. Krimmel, H.-A. Krug von Nidda, V. Tsurkan, and A. Loidl, Phys. Rev. B **72**, 174404 (2005).

[9] A. Krimmel, H. Mutka, M. M. Koza, V. Tsurkan, and A. Loidl, Phys. Rev. B **79**, 134406 (2009).

[10] V. Fritsch, J. Hemberger, N. Büttgen, E.-W. Scheidt, H.-A. Krug von Nidda, A. Loidl, and V. Tsurkan, Phys. Rev. Lett. **92**, 116401 (2004).

[11] S. Gao, O. Zaharko, V. Tsurkan, Y. Su, J. S. White, G. S. Tucker, B. Roessli, F. Bourdarot, R. Sibille, D. Chernyshov, *et al.*, Nature physics **13**, 157 (2017).

[12] K. Guratinder, V. Tsurkan, L. Prodan, L. Keller, J. P. Embs, F. Juranyi, M. Medarde, C. Rüegg, and O. Zaharko, Phys. Rev. B **105**, 174423 (2022).

[13] L. Ge, J. Flynn, J. A. M. Paddison, M. B. Stone, S. Calder, M. A. Subramanian, A. P. Ramirez, and M. Mourigal, Phys. Rev. B **96**, 064413 (2017).

[14] J. R. Chamorro, L. Ge, J. Flynn, M. A. Subramanian, M. Mourigal, and T. M. McQueen, Phys. Rev. Materials **2**, 034404 (2018).

[15] M. M. Bordelon, C. Liu, L. Posthuma, E. Kenney, M. J. Graf, N. P. Butch, A. Banerjee, S. Calder, L. Balents, and S. D. Wilson, Phys. Rev. B **103**, 014420 (2021).

[16] M. M. Bordelon, J. D. Bocarsly, L. Posthuma, A. Banerjee, Q. Zhang, and S. D. Wilson, Phys. Rev. B **103**, 024430 (2021).

[17] G. Chen, L. Balents, and A. P. Schnyder, Phys. Rev. Lett. **102**, 096406 (2009).

[18] L. Savary, E. Gull, S. Trebst, J. Alicea, D. Bergman, and L. Balents, Phys. Rev. B **84**, 064438 (2011).

[19] H. S. Nair, Z. Fu, J. Voigt, Y. Su, and T. Brückel, Phys. Rev. B **89**, 174431 (2014).

[20] G. J. MacDougall, A. A. Aczel, Y. Su, W. Schweika, E. Faulhaber, A. Schneidewind, A. D. Christianson, J. L. Zarestky, H. D. Zhou, D. Mandrus, and S. E. Nagler, Phys. Rev. B **94**, 184422 (2016).

[21] K. W. Plumb, J. R. Morey, J. A. Rodriguez-Rivera, H. Wu, A. A. Podlesnyak, T. M. McQueen, and C. L. Broholm, Phys. Rev. X **6**, 041055 (2016).

[22] A. Biffin, C. Rüegg, J. Embs, T. Guidi, D. Cheptiakov, A. Loidl, V. Tsurkan, and R. Coldea, Phys. Rev. Lett. **118**, 067205 (2017).

[23] V. Tsurkan, L. Prodan, V. Felea, I. Filippova, V. Kravtsov, A. Günther, S. Widmann, H.-A. Krug von Nidda, J. Deisenhofer, and A. Loidl, Phys. Rev. B **96**, 054417 (2017).

[24] T. Naka, J. Valenta, J. Kaštil, M. Míšek, J. Prchal, V. Sechovský, H. Abe, T. Nakane, M. Nakayama, and T. Uchikoshi, Materials Research Express **7**, 056105 (2020).

[25] H. Cho, C. H. Kim, Y. Lee, K. Komatsu, B.-G. Cho, D.-Y. Cho, T. Kim, C. Kim, Y. Kim, T. Y. Koo, Y. Noda, H. Kagi, D. I. Khomskii, D. Seoung, and J.-G. Park, Phys. Rev. B **103**, L081101 (2021).

[26] F.-Y. Li and G. Chen, Phys. Rev. B **98**, 045109 (2018).

[27] J. Q. Liu, F.-Y. Li, G. Chen, and Z. Wang, Phys. Rev. Research **2**, 033260 (2020).

[28] J. R. Morey, A. Scheie, J. P. Sheckelton, C. M. Brown, and T. M. McQueen, Phys. Rev. Materials **3**, 014410 (2019).

[29] C. Wang, A. Nahum, and T. Senthil, Phys. Rev. B **91**, 195131 (2015).

[30] F. L. Buessen, M. Hering, J. Reuther, and S. Trebst, Phys. Rev. Lett. **120**, 057201 (2018).

[31] G. Chen, Phys. Rev. B **96**, 020412(R) (2017).

[32] F.-Y. Li and G. Chen, Phys. Rev. B **100**, 045103 (2019).

[33] S. Horiuti and S. Miyahara, Journal of the Physical Society of Japan **19**, 423 (1964).

[34] G. Blasse and D. Schipper, Physics Letters **5**, 300 (1963).

[35] S. Das, D. Nafday, T. Saha-Dasgupta, and A. Paramekanti, Phys. Rev. B **100**, 140408(R) (2019).

[36] Y. Wang, G. Fabbris, M. Dean, and G. Kotliar, Computer Physics Communications **243**, 151 (2019).

[37] See Supplemental Material for details on the RIXS cross section calculations.

[38] R. D. Cowan, *The Theory of Atomic Structure and Spectra* (Univ of California Press, 1981).

[39] P. Gütlich, K. M. Hasselbach, H. Rummel, and H. Spiering, The Journal of Chemical Physics **81**, 1396 (1984).

[40] V. Kocsis, S. Bordács, D. Varjas, K. Penc, A. Abouelsayed, C. A. Kuntscher, K. Ohgushi, Y. Tokura, and I. Kézsmárki, Phys. Rev. B **87**, 064416 (2013).

[41] F. de Groot, Journal of Electron Spectroscopy and Related Phenomena **67**, 529 (1994).

[42] E. Z. Kurmaev, R. G. Wilks, A. Moewes, L. D. Finkelstein, S. N. Shamin, and J. Kuneš, Phys. Rev. B **77**, 165127 (2008).

[43] M. J. Wahila, Z. W. Lebens-Higgins, A. J. Jackson, D. O. Scanlon, T.-L. Lee, J. Zhang, K. H. L. Zhang, and L. F. J. Piper, Phys. Rev. B **100**, 085126 (2019).

[44] F. Frati, M. O. Hunault, and F. M. de Groot, Chemical reviews **120**, 4056 (2020).

[45] M. Lenglet, Materials Research Bulletin **35**, 531 (2000).

[46] I. Mayer and S. Angelov, physica status solidi (b) **106**, 467 (1981).

[47] M. Zhu, D. Do, C. R. Dela Cruz, Z. Dun, J.-G. Cheng, H. Goto, Y. Uwatoko, T. Zou, H. D. Zhou, S. D. Mahanti, and X. Ke, Phys. Rev. B **92**, 094419 (2015).

[48] V. M. Katukuri, P. Babkevich, O. Mustonen, H. C. Walker, B. Fåk, S. Vasala, M. Karppinen, H. M. Rønnow, and O. V. Yazyev, Phys. Rev. Lett. **124**, 077202 (2020).

[49] F. Bahrami, X. Hu, Y. Du, O. I. Lebedev, C. Wang, H. Luetkens, G. Fabbris, M. J. Graf, D. Haskel, Y. Ran, and F. Tafti, Science Advances **8**, eabl5671 (2022).

[50] T. Burnus, Z. Hu, H. Wu, J. C. Cezar, S. Niitaka, H. Takagi, C. F. Chang, N. B. Brookes, H.-J. Lin, L. Y. Jang, A. Tanaka, K. S. Liang, C. T. Chen, and L. H. Tjeng, Phys. Rev. B **77**, 205111 (2008).

[51] J. P. Clancy, A. Lupascu, H. Gretarsson, Z. Islam, Y. F. Hu, D. Casa, C. S. Nelson, S. C. LaMarra, G. Cao, and Y.-J. Kim, Phys. Rev. B **89**, 054409 (2014).

[52] S. Chikara, G. Fabbris, J. Terzic, G. Cao, D. Khomskii, and D. Haskel, Phys. Rev. B **95**, 060407(R) (2017).

[53] Y. Wu and D. E. Ellis, Journal of Physics: Condensed Matter **7**, 3973 (1995).

[54] D. Meyers, S. Middey, J.-G. Cheng, S. Mukherjee, B. Gray, Y. Cao, J.-S. Zhou, J. Goodenough, Y. Choi, D. Haskel, *et al.*, Nature communications **5**, 1 (2014).

[55] M. Kobayashi, M. Seki, M. Suzuki, R. Okano, M. Kitamura, K. Horiba, H. Kumigashira, A. Fujimori, M. Tanaka, and H. Tabata, Phys. Rev. B **105**, 205103 (2022).

[56] K. Takubo, S. Hirata, J.-Y. Son, J. W. Quilty, T. Mizokawa, N. Matsumoto, and S. Nagata, Phys. Rev. Lett. **95**, 246401 (2005).

[57] W. F. J. Fontijn, P. J. van der Zaag, L. F. Feiner, R. Metselaar, and M. A. C. Devillers, Journal of Applied Physics **85**, 5100 (1999).

[58] K. J. Kim, H. S. Lee, M. H. Lee, and S. H. Lee, Journal of Applied Physics **91**, 9974 (2002).

[59] A. Agui, T. Uozumi, M. Mizumaki, and T. Käämbre, Phys. Rev. B **79**, 092402 (2009).

[60] S. G. Chiuzbăian, S. Brignolo, C. F. Hague, R. Delaunay, M. Guarise, A. Nicolaou, Z. Yang, H. Zhou, and J.-M. Mariot, The Journal of Physical Chemistry C **121**, 22369 (2017).

[61] B. Liu, E. N. Glass, R.-P. Wang, Y.-T. Cui, Y. Harada, D.-J. Huang, S. Schuppler, C. L. Hill, and F. M. F.

de Groot, Phys. Chem. Chem. Phys. **20**, 4554 (2018).

[62] R. J. Green, M. W. Haverkort, and G. A. Sawatzky, Phys. Rev. B **94**, 195127 (2016).

[63] E. B. Guedes, F. Abud, H. P. Martins, M. Abbate, R. F. Jardim, and R. J. O. Mossanek, Phys. Rev. B **100**, 075132 (2019).

[64] M. W. Haverkort, M. Zwierzycki, and O. K. Andersen, Phys. Rev. B **85**, 165113 (2012).

[65] V. Kocsis, S. Bordács, J. Deisenhofer, L. F. Kiss, K. Ohgushi, Y. Kaneko, Y. Tokura, and I. Kézsmárki, Phys. Rev. B **97**, 125140 (2018).

[66] A. Krimmel, M. Mücksch, V. Tsurkan, M. M. Koza, H. Mutka, and A. Loidl, Phys. Rev. Lett. **94**, 237402 (2005).

[67] M. Ptak, M. Maczka, A. Gągor, A. Pikul, L. Macalik, and J. Hanuza, Journal of Solid State Chemistry **201**, 270 (2013).

[68] Z. Wang, S. Saxena, P. Lazor, and H. O'Neill, Journal of Physics and Chemistry of Solids **64**, 425 (2003).

[69] A. Geondzhian, A. Sambri, G. M. De Luca, R. Di Capua, E. Di Gennaro, D. Betto, M. Rossi, Y. Y. Peng, R. Fumagalli, N. B. Brookes, L. Braicovich, K. Gilmore, G. Ghiringhelli, and M. Salluzzo, Phys. Rev. Lett. **125**, 126401 (2020).

[70] T. Saha-Dasgupta, Materials Research Express **7**, 014003 (2020).

[71] M.-C. Lee, S. Lee, C. J. Won, K. D. Lee, N. Hur, J.-L. Chen, D.-Y. Cho, and T. W. Noh, Phys. Rev. B **97**, 125123 (2018).

[72] K. Park, G. L. Pascut, G. Khanal, M. O. Yokosuk, X. Xu, B. Gao, M. J. Gutmann, A. P. Litvinchuk, V. Kiryukhin, S. W. Cheong, D. Vanderbilt, K. Haule, and J. L. Musfeldt, Phys. Rev. B **104**, 195143 (2021).

[73] L. Xu, N. A. Bogdanov, A. Princep, P. Fulde, J. Van Den Brink, and L. Hozoi, npj Quantum Materials **1**, 1 (2016).

[74] H. Huang, A. Singh, C. Wu, J. Xie, J. Okamoto, A. Belik, E. Kurmaev, A. Fujimori, C. Chen, S. Streltsov, *et al.*, npj Quantum Materials **7**, 1 (2022).

[75] W. Jin, S. H. Chun, J. Kim, D. Casa, J. P. C. Ruff, C. J. Won, K. D. Lee, N. Hur, and Y.-J. Kim, Phys. Rev. B **105**, 054419 (2022).

[76] A. Smerald and G. Jackeli, Phys. Rev. Lett. **122**, 227202 (2019).

[77] K. Amelin, Y. Alexanian, U. Nagel, T. Rõõm, J. Robert, J. Debray, V. Simonet, C. Decorse, Z. Wang, R. Ballou, E. Constable, and S. de Brion, Phys. Rev. B **102**, 134428 (2020).

[78] A. Marciniak, S. Marcantoni, F. Giusti, F. Glerean, G. Sparapassi, T. Nova, A. Cartella, S. Latini, F. Valiera, A. Rubio, *et al.*, Nature Physics **17**, 368 (2021).

[79] D. Afanasiev, J. Hortensius, B. Ivanov, A. Sasani, E. Bousquet, Y. Blanter, R. Mikhaylovskiy, A. Kimel, and A. Caviglia, Nature materials **20**, 607 (2021).

[80] E. Ergeçen, B. Ilyas, D. Mao, H. C. Po, M. B. Yilmaz, J. Kim, J.-G. Park, T. Senthil, and N. Gedik, Nature Communications **13**, 1 (2022).